Check for updates

Thermodynamics of a deeply degenerate SU(*N*)-symmetric Fermi gas

Lindsay Sonderhouse [1,4] ✉, Christian Sanner[1,4], Ross B. Hutson[1], Akihisa Goban[1,3], Thomas Bilitewski [1,2], Lingfeng Yan[1], William R. Milner[1], Ana M. Rey [1,2] and Jun Ye [1] ✉

Many-body quantum systems can exhibit a striking degree of symmetry unparalleled in their classical counterparts. In real materials SU(*N*) symmetry is an idealization, but this symmetry is pristinely realized in fully controllable ultracold alkaline-earth atomic gases. Here, we study an SU(*N*)-symmetric Fermi liquid of ^{87}Sr atoms, where *N* can be tuned to be as large as 10. In the deeply degenerate regime, we show through precise measurements of density fluctuations and expansion dynamics that the large *N* of spin states under SU(*N*) symmetry leads to pronounced interaction effects in a system with a nominally negligible interaction parameter. Accounting for these effects, we demonstrate thermometry accurate to 1% of the Fermi energy. We also demonstrate record speed for preparing degenerate Fermi seas enabled by the SU(*N*)-symmetric interactions, reaching $T/T_F = 0.22$ with 10 nuclear spin states in 0.6 s working with a laser-cooled sample. This, along with the introduction of a new spin polarizing method, enables the operation of a three-dimensional optical lattice clock in the band insulating regime.

Modern quantum science strives to understand and harness the rich physics underlying interacting many-particle systems. In particular, ultracold quantum gases have been established as ideal model systems with which to explore open questions in condensed matter physics ranging from understanding superconductivity to realizing highly correlated states and exotic phases of matter[1,2]. It is often the interplay of interactions and symmetries that shapes the complex behaviour in these quantum many-body systems[3].

The dominant interactions at ultralow temperatures in quantum gases occur via *s*-wave contact scattering, which, for identical fermions, vanishes due to the antisymmetry of fermionic wavefunctions. Therefore, multicomponent gases are required to realize interacting Fermi systems. Whereas binary mixtures are well-studied, versatile platforms for quantum simulation capable of exploring a wide parameter space[4,5], the additional freedom in choosing the number of spin components, *N*, offers unique, largely unexplored opportunities.

In alkaline-earth fermionic atoms, the complete decoupling between the nuclear and electronic degrees of freedom intrinsic to their internal ground state manifold gives rise to perfectly SU(*N*)-symmetric two-body interactions, characterized by a single nuclear-spin-independent scattering length *a*. This raises the question of the extent to which this enlarged symmetry enriches the many-body behaviour, and how it affects the thermodynamic and statistical properties of the quantum gas as *N* is increased.

Although recent studies have started to investigate the intriguing properties of SU(*N*) quantum matter, most of the effort so far has been concentrated on the investigation of lattice-confined gases[3,6–11]. Experiments probing the role of SU(*N*) interactions in a regime where a Fermi liquid description is accurate have been limited to non-degenerate[12] or only slightly degenerate gases[13–16]. Here, we explore a deeply degenerate regime where *N* Fermi seas coexist and fundamentally modify the system's thermodynamics (Fig. 1).

In addition to enriching the system's quantum behaviour, SU(*N*) symmetry is an untapped resource for cooling[7,17–19]. It can enhance the collision and thermalization rate during evaporative cooling without inelastic spin collisions and thus provide a tool with which to efficiently remove entropy from the system.

In this work, we study a deeply degenerate SU(*N*) symmetric ^{87}Sr Fermi gas with $N \leq 10$. We show how the large number of nuclear spin states enables an unprecedented short preparation time to reach Fermi degeneracy with a temperature $T/T_F = 0.22$, where T_F is the Fermi temperature, achieved in just 0.6 s of evaporation with a laser-cooled sample. We use the rapid preparation and deep degeneracy to study the pronounced modifications introduced by SU(*N*) interactions on the thermodynamic properties of the gas[20]. In particular, we experimentally demonstrate and theoretically validate within a kinetic approach the effects of SU(*N*) interactions on the density profile, number fluctuations and compressibility, as well as the time-of-flight dynamics of the gas. Our study paves the way for future investigation of SU(*N*) interactions in regimes where even richer physics emerges and Fermi liquid theory becomes invalid. Furthermore, we introduce a Stark-shift-enabled spin selection technique to spin-polarize deeply degenerate gases, allowing efficient preparation of a low-entropy Fermi gas that is invaluable for further development of a quantum degenerate 3D lattice clock[21,22]. Our spin selection technique improves the stability of state-of-the-art optical clocks, which are limited at present by the time spent preparing the system[23–29]. This is particularly relevant in the context of recently proposed lattice clocks that rely on engineered quantum states of matter[30].

Fast preparation

Our preparation scheme (Fig. 2a) begins with standard laser-cooling techniques developed for alkaline-earth atoms[31]. After two stages of laser cooling, roughly 10^7 atoms are cooled to $2\,\mu K$ in a far-off-resonant crossed optical dipole trap (XODT) with a sheet-like geometry[21,32]. A vertically oriented round optical dipole trap (VODT) forms a dimple in a horizontal optical sheet potential that is provided by an elliptically shaped horizontal optical dipole
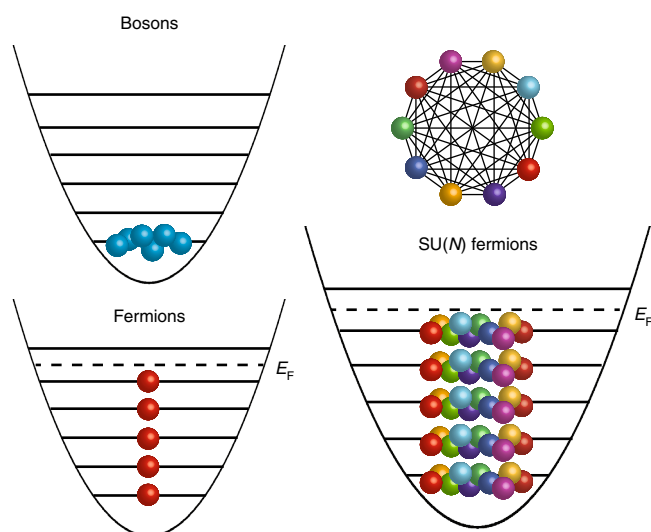
Fig. 1 | Degenerate bosons, fermions and SU(N) fermions. Unlike bosons, which can occupy the same state, indistinguishable fermions must separate into different energy levels. SU(N) fermions, on the other hand, can have N particles per state. In a given level, each particle has (N−1) distinct partners, as shown in the top right, and interactions are correspondingly enhanced.

trap (HODT) (Fig. 2c). The HODT provides support against gravity and therefore determines the effective trap depth.

The density obtainable in a magneto-optical trap (MOT) is generally limited by inelastic light-assisted collisions[33] and reabsorption of the cooling light, which leads to an effective repulsion between atoms[34]. To increase the density inside the dimple beyond these limits, we locally apply an additional laser that renders atoms inside the dimple region transparent to MOT light, a method that was adapted from bosonic ^{84}Sr (ref. [35]). The beam spatially overlaps with the VODT but has a slightly larger waist. This 'transparency' laser shifts the cooling light out of resonance, and a high density can then be reached inside the dimple, where atoms collect. Atoms in the dimple thermalize with atoms in a large reservoir part of the trap, which are continually being cooled by the MOT light.

The transparency beam has allowed the production of Bose–Einstein condensation without further evaporation[35]. However, for fermions other complications can arise. Compared with bosonic strontium, ^{87}Sr has additional hyperfine structure, creating a different a.c. Stark shift for each nuclear sublevel. Transparency from both the trapping and stirring second-stage MOT lasers is also required[36]. Accordingly, we use transparency light that is blue-detuned by 25 GHz from the $^3P_1$–$^3S_1$ transition (Fig. 2b). This provides an ample shift for all nuclear spin states and keeps spontaneous scattering events beyond relevant experimental timescales. The beam is linearly polarized and perpendicular to the magnetic quantization field, which is applied along gravity. With this geometry, the smallest Stark shift still detunes the excited state by 250 linewidths. After 400 ms of cooling with the transparency beam, the number of atoms in the dimple saturates with 5×10^6 atoms (that is, about 50% of the total atom number), a temperature of 2 μK and $T/T_F = 1.9$ (see Methods). Lower temperatures can be achieved by adjusting the MOT light; however, the phase-space density does not improve.

The very dense and almost degenerate sample can then be further cooled via forced evaporation. Spin relaxation is absent due to the SU(N)-symmetric nature of ^{87}Sr in the $^1S_0$ ground state; however, over the timescale of seconds, we observe a decay of the sample that

is well described by a three-body loss process with a three-body loss coefficient $k_3 = 4.7(1.2) \times 10^{-30}\,\mathrm{cm}^6\,\mathrm{s}^{-1}$ (see Methods).

The elastic collision rate[37] for a non-degenerate, balanced spin mixture is proportional to $(1 - 1/N)\,N\overline{n}_\sigma$, where $\overline{n}_\sigma$ is the spatially averaged density for spin state σ. Assuming a constant total atom number, it is thus advantageous to have all ten spin states populated. We reach an initial collision rate of $1{,}000\,\mathrm{s}^{-1}$ with $N = 10$. Evaporation begins at a trap depth of 20 μK with radial trap frequency ν_r and vertical trap frequency ν_z in the dimple of $(\nu_r, \nu_z) = (100, 800)$ Hz. The HODT intensity is then reduced in a two-stage ramp down to a final trap depth of a few 100 nK with trap frequencies of (100, 200) Hz.

After 600 ms of evaporation, we reach $T/T_F = 0.22$ with 3×10^4 atoms per spin state. Slower evaporation leads to lower temperatures, and we achieve $T/T_F = 0.07$ with 5×10^4 atoms per spin state after evaporating for 2.4 s. This marks a considerable improvement over previous evaporation results, where evaporation stages took around 10 s (ref. [21]), limiting the potential of Fermi-degenerate optical atomic clocks[38].

We observe an approximate $1/(N-1)$ scaling of the total evaporation time with the number of spin states participating in evaporation as shown in Fig. 2d, reflecting the reduction in collisional partners for smaller N. Here, each sample is prepared with the same atom number per spin state and T/T_F, and is measured after reaching $T/T_F = 0.12$. The final atom number per spin state changes by roughly a factor of two as N varies.

Spin manipulation

To manipulate the spin composition of the atom sample and prepare a spin-polarized gas, we apply a spin-selective optical potential to the atoms after evaporation. Past procedures have used optical Stern–Gerlach techniques to separate out spin states during the time of flight[39–41], but our method, the tensor Stark shift spin selector (TenS4), creates a spin-selective force on the atoms from the tensor Stark shift of a laser while the atoms remain trapped in the XODT. Atoms with the same magnitude of the nuclear spin state $|m_F|$, where m_F represents the projection of the total angular momentum F along the quantization axis, experience a small differential force due to an applied magnetic field of 5 G. This magnetic field is too small to fully remove $m_F = -9/2$ and $-7/2$. We thus conventionally remove these spins via optical pumping before evaporative cooling. The TenS4 beam is offset from the atoms such that the a.c. Stark shift varies across the atomic sample by hundreds of nanokelvin, which causes a spin-dependent modification in the combined optical and gravitational potential of the atoms (Fig. 2e). The TenS4 laser is blue-detuned from the $^3P_1$, $F = 11/2$ transition by 266 MHz (Fig. 2b), where the polarizability from $^3P_1$, $F = 11/2$ cancels the polarizability from $^3P_1$, $F = 9/2$ for nuclear spin state $m_F = +9/2$. As a result, atoms with $m_F = +9/2$ are unaffected by the TenS4 laser, whereas all other spin states are subject to a repelling force. A detailed experimental protocol is provided in the Methods.

The spin purity after applying the TenS4 laser for 10 ms is measured by loading the atoms into a deep 3D optical lattice. The spin population for each nuclear spin state is then read out through selective π-pulse excitations on the clock transition. We measure 92% of the atoms in the target $m_F = +9/2$ state, as shown in Fig. 2f, and an atom number of 3.3×10^4 after the TenS4 beam is applied, in rough agreement with one-eighth of the initial atom population of 2.5×10^5. The temperature of the sample increases by only ~10%. Our technique provides spin-state selectivity without optical excitation and, as a result, does not cause light-induced heating, overcoming issues typically associated with optical pumping schemes. The spin distillation technique enables us to load a single spin with $T/T_F = 0.2$ into a 3D optical lattice with a total preparation time under 3 s (Fig. 2a).

Characterization of SU(N)-enhanced interactions

Having prepared a high-density, deeply degenerate SU(10) gas, we demonstrate in the following that a nominally very weakly
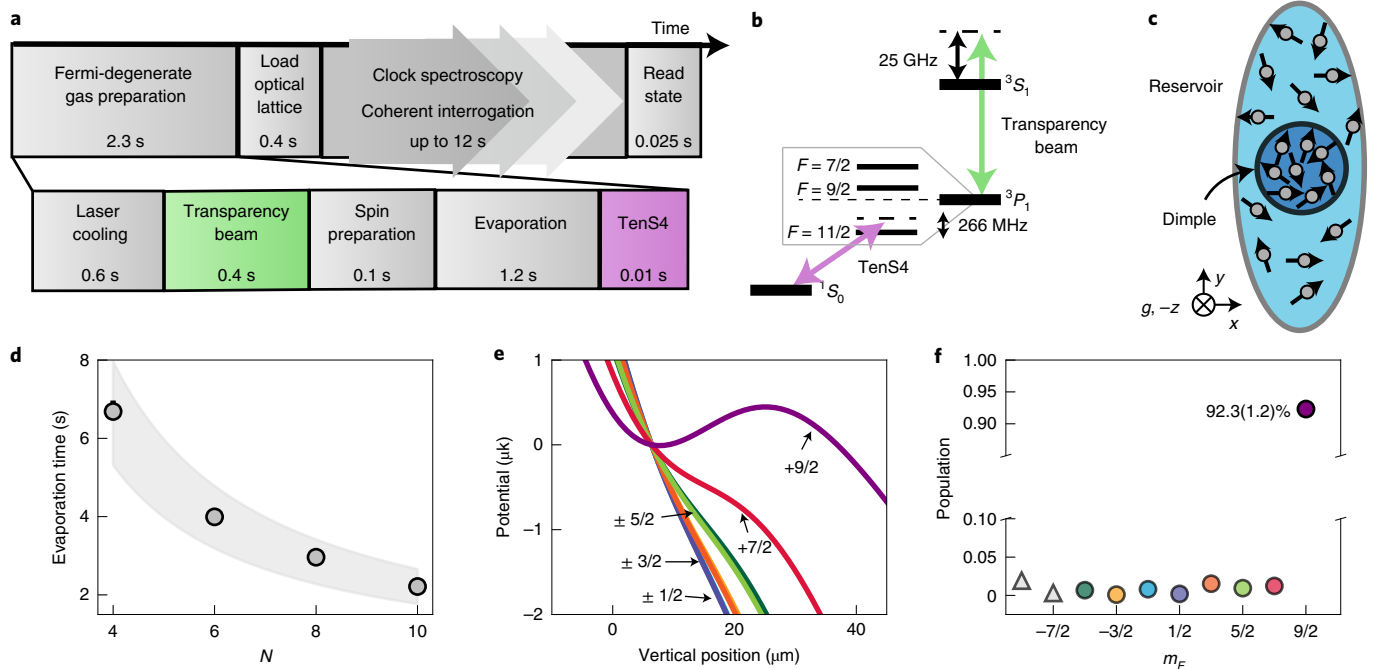
Fig. 2 | Preparation of a degenerate Fermi gas. a, Timing diagram showing the stages of the experimental sequence. The times are optimized for clock operation in the band insulating regime. Single spin samples with 20,000 atoms at $T/T_F = 0.2$ are prepared in a 3D optical lattice in under 3 s. **b**, Level diagram depicting the energy transitions for the transparency beam (green) and TenS4 (purple). **c**, Atoms are confined in an XODT consisting of a reservoir and dimple trap, and accumulate in the dimple after a transparency laser is applied. The transparency and TenS4 lasers overlap with the dimple, and form a 10° angle with respect to gravity. **d**, Time to reach $T/T_F = 0.12$ for different numbers of nuclear spin states N participating in evaporation. Each trajectory is prepared with $9.6(8) \times 10^5$ atoms per spin state and $T/T_F = 2.0(1)$, where the error represents the maximum deviation. The grey band denotes a $1/(N-1)$ scaling based on the number of initial collisional partners, given a $\pm 20\%$ change in the atom number. The error bars are upper bounds, reflecting the resolution of the sampling grid, and are smaller than the marker size. **e**, Combined optical and gravitational potential after application of the TenS4 laser. The beam creates a spin-dependent modification of the potential, and only atoms in spin state $m_F = +9/2$ (purple line) are supported against gravity. Atoms in $m_F = -9/2$ and $-7/2$ are removed through optical pumping. **f**, Spin purity after application of the TenS4 laser for 10 ms. Atoms are loaded into a 3D optical lattice and the spin state population is determined using selective excitation on the ultranarrow $^1S_0$–$^3P_0$ transition. Grey triangles correspond to spin states that are removed through optical pumping. The error bars denote the standard error of the mean (s.e.m.) and are smaller than the marker size.

interacting quantum system with interaction parameter $k_F a \ll 1$, where k_F is the magnitude of the Fermi wave vector, can develop striking interaction effects due to SU(N) enhancement. The nuclear spin degree of freedom substantially modifies the character of the gas towards an interacting multicomponent Fermi liquid with subtle consequences for correlation analysis and thermometry.

To investigate this intriguing quantum system and illuminate the role of SU(N) symmetry, we perform measurements that characterize the system's thermodynamics. A key quantity in this context is the isothermal compressibility $\kappa = \frac{1}{n^2} \frac{\partial n}{\partial \mu}$, where $n = N n_\sigma$ denotes the particle density and μ the chemical potential. For ^{87}Sr with $a = 97 a_{Bohr}$, where a_{Bohr} is the atomic Bohr radius, the contact interactions are repulsive and a decreased compressibility would be expected compared with an ideal Fermi gas with compressibility κ_0. For a homogeneous gas in the zero-temperature limit where $\kappa_0 = 3/(2N n_\sigma E_F)$ with Fermi energy E_F and Fermi wave vector $k_F = (6\pi^2 n_\sigma)^{1/3}$, one finds to first order in $k_F a$ the ratio $\kappa_0/\kappa = 1 + (N-1)2k_F a/\pi$ (ref. [20]). Therefore, the symmetric N-component system is effectively $(N-1)$-fold more repulsive than a typical two-spin-component Fermi liquid[42]. The favourable scaling with number of internal levels has to be contrasted with the weak dependence of the compressibility on the atom number per spin state in a harmonically trapped gas, where $k_F \propto N_\sigma^{1/6}$. All experiments reported in the following were carried out with spin-balanced ten-component samples. By focusing on this maximum N limit, we achieve pronounced interaction effects and can perform sensitive experiment–theory comparisons.

Experimentally, we access the compressibility of the gas by measuring its local density fluctuations. Fluctuations, either thermal or quantum, are the drivers of phase transitions, and are sensitive to the underlying phase of matter, its quasi-particles and interactions. The fluctuation–dissipation theorem states that the thermally driven fluctuations of a thermodynamic variable are fundamentally related to the conjugate external force through the susceptibility[43]. Considering a small subvolume of the gas cloud containing on average $\tilde{N}$ atoms, the corresponding generalized force is the local chemical potential μ. The relative number fluctuations $\eta = \Delta \tilde{N}^2 / \tilde{N}$ are therefore related to the susceptibility $\partial \tilde{N}/\partial \mu$ via $\eta = n k_B T \kappa$, where k_B is the Boltzmann constant. Although the equation of state of a classical ideal gas dictates that $\eta = 1$, a value of $\eta = 3/2 \, T/T_F$ would be expected for a deeply degenerate ideal Fermi gas. These sub-Poissonian fluctuations reflect the degeneracy pressure in the gas. Combined with the compressibility reduction due to repulsive interactions, it would be expected, to first order in temperature and interactions (see Methods), that:

$$\eta = \frac{3}{2} \frac{T/T_F}{1 + \frac{2}{\pi} (k_F a)(N-1)},$$

which suggests that even in the $k_F a \ll 1$ limit the interaction effects become non-negligible due to the $(N-1)$-fold SU(N) enhancement.

Our density fluctuation measurements are performed on expanded gas clouds. After abruptly turning off the harmonic confinement ($\nu_r = 130$ Hz, $\nu_z = 240$ Hz) the quantum degenerate sample
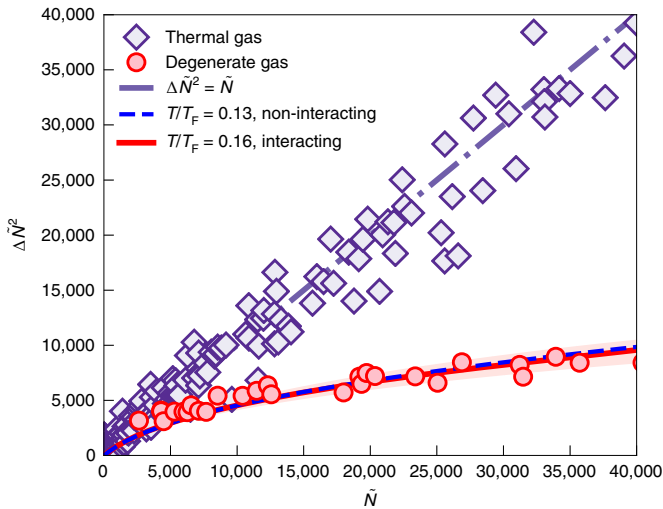
Fig. 3 | Local density fluctuations of an SU(N) degenerate gas. Density fluctuations after 11.5 ms time of flight for a degenerate cloud with $N = 10$ nuclear spin states. The data are fitted using an SU(N) interacting model to extract $T/T_F = 0.16$, with shading representing a 2σ uncertainty of $\pm 0.02\, T/T_F$. Fitting the data instead to a non-interacting ideal Fermi gas gives $T/T_F = 0.13$, showing an interaction-induced suppression of ~20%. The difference between the interacting and non-interacting fits is much less than the scatter in the data, highlighting the indistinguishability between interacting and non-interacting systems when measuring density fluctuations alone at the given signal-to-noise ratio. The total density fluctuations are 25% of that of the thermal gas. A thermal cloud reproduces Poisson statistics with $\Delta \tilde{N}^2 / \tilde{N} = 1$. Each data point is obtained by looking at the atom number variation and mean in a subregion of the cloud for a series of images.

that contains in total $10 \times 59{,}000$ atoms such that $k_F a = 0.07$ freely expands over 11.5 ms. We then obtain line-of-sight integrated density profiles via absorption imaging. Following the protocol described in refs. [44,45], we run this experiment in a repeated fashion so that for each projected subregion of the cloud containing $\tilde{N}$ atoms we can measure the statistical variance $\Delta \tilde{N}^2$. Figure 3 shows the results obtained from 400 individual images together with a calibration line derived from noise measurements on a thermal gas. Pronounced noise suppression down to about 25% of thermal noise in the centre of the sample indicates that the gas is deeply in the quantum regime.

To quantitatively interpret the noise data beyond first order and decouple Pauli suppression and SU(N)-enhanced interaction contributions, we calculate the expected line-of-sight integrated number fluctuations based on a kinetic approach[46,47], using the collisional Boltzmann–Vlasov equation with a mean-field interaction term. The Boltzmann–Vlasov equation describes the evolution of the semi-classical phase-space distribution $f(\mathbf{r}, \mathbf{p})$ with position $\mathbf{r}$ and momentum $\mathbf{p}$:

$$\left(\partial_t + \frac{\mathbf{p}}{m} \cdot \nabla_\mathbf{r} - \nabla_\mathbf{r}[U(\mathbf{r}) + V_{MF}(\mathbf{r})] \cdot \nabla_\mathbf{p} \right) f = I_c(f) . \quad (1)$$

The phase-space distribution evolves due to ballistic motion (second term), forces from the harmonic trapping potential $U = m/2 \sum_i (2\pi \nu_i)^2 r_i^2$, mean-field interactions with strength $V_{MF} = g(N-1)n$ where $g = 4\pi \hbar^2 a/m$, and collisions that are described by the integral $I_c(f)$ (see Methods)[47,48]. Solving the Boltzmann–Vlasov equation in equilibrium and for finite temperature allows us to obtain the real-space density, n, from which we can compute the compressibility and thus the number fluctuations in trap and after time of flight. By fitting this model to the observed fluctuations, we extract $T/T_F = 0.16 \pm 0.01$. At these low temperatures, $I_c(f)$ plays no role.
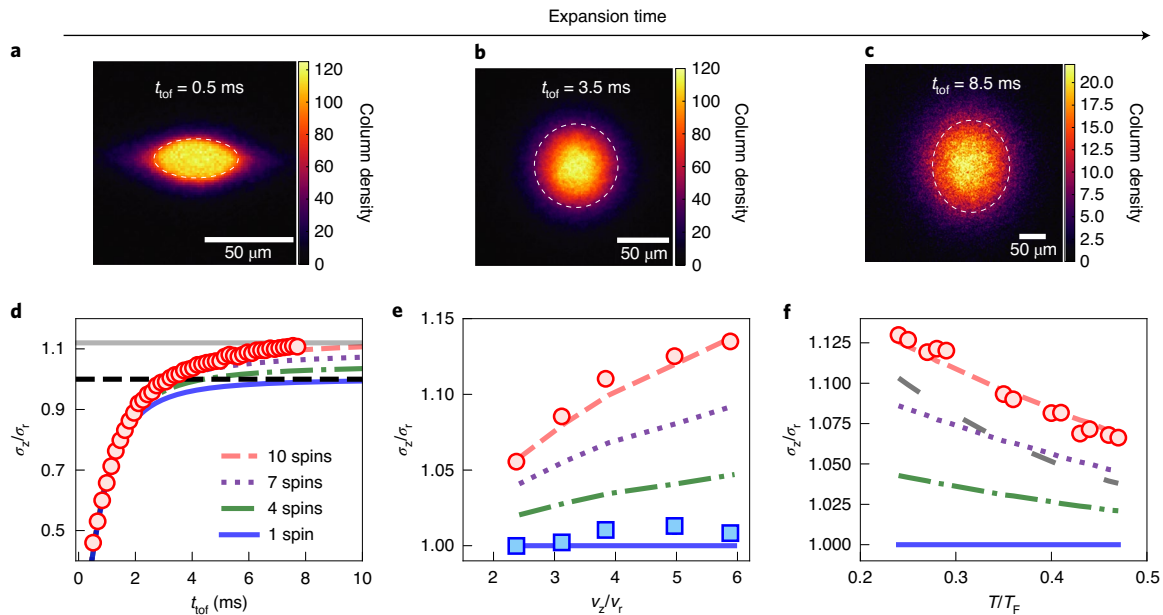
Expansion time →

Fig. 4 | Cloud anisotropy. a–c, Line-of-sight integrated atomic density for t_{tof} of 0.5 ms (**a**), 3.5 ms (**b**) and 8.5 ms (**c**) in terms of the number of atoms per 1.37 μm^2. **d,** Aspect ratio of a cloud of cold atoms with $N = 10$ nuclear spin states released from an XODT for variable expansion times (red circles). Here, σ_z (σ_r) represents the vertical (horizontal) $1/e^2$ Gaussian width of the cloud. An identical aspect ratio is extracted using a Fermi–Dirac fit. After ~3 ms, the aspect ratio passes through unity (black dashed line), a clear signature of interactions in the gas. At long timescales, the sample approaches an aspect ratio of 1.12 (grey line). The sample has an initial trap asymmetry of $\nu_z/\nu_r = 6.4$. **e,** Aspect ratio versus initial trap asymmetry of a degenerate gas for $N = 10$ (red circles) and $N = 1$ (blue squares) after time-of-flight expansion for 15.5 ms. **f,** Aspect ratio versus temperature. Data are shown with roughly the same atom number per shot. The data are fitted using an interacting model that includes both a mean-field interaction and an additional collisional term. Neglecting the collisional term fails to explain the results (grey dashed line). All error bars represent the s.e.m. and are smaller than the data points.
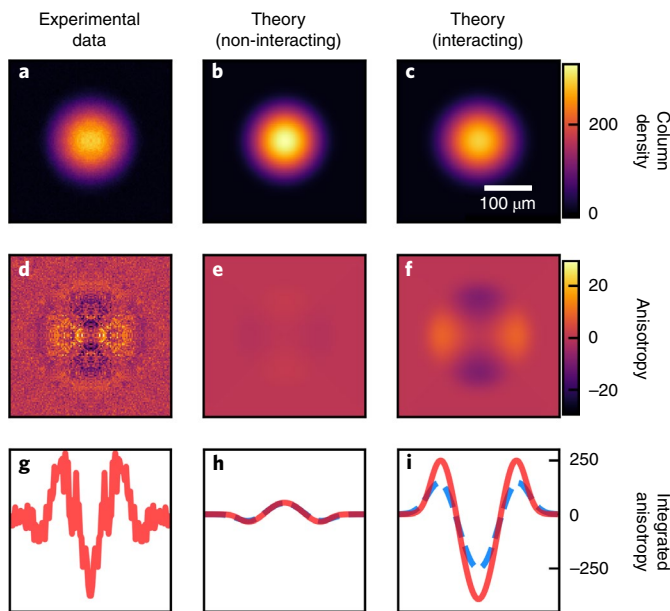
Fig. 5 | Interaction signatures. a–c, Line-of-sight integrated atomic density $n(x, z)$ after time-of-flight for a single shot of the experimental data (**a**), non-interacting theory (**b**) and interacting theory (**c**), respectively. The colour scales represent the numbers of atoms per 1.37 µm². Images are shown with an initial trap asymmetry of $\nu_z/\nu_r = 1.8$ and $T/T_F = 0.17$. **d–f**, The corresponding anisotropy of the cloud, defined as $n(x, z) - n(z, x)$; lobes are clearly visible for clouds with interactions. To improve the signal-to-noise ratio, the experimental image is first symmetrized by reflection along the x and z axes. **g–i**, If the anisotropy is integrated along one direction, peaks symmetric to the centre of the gas that are sensitive to temperature appear for both the experimental data (**g**) and the interacting distribution (**i**), whereas the non-interacting signal (**h**) shows a different signature that displays only weak temperature dependence. The red lines show the integrated anisotropy of the images in (**d–f**), whereas the dashed blue lines in **h** and **i** show the integrated profile for a temperature that is 50% higher.

To illustrate the interaction-induced compressibility change, we also fit a non-interacting model to the noise data, which gives an apparent $T/T_F = 0.13 \pm 0.01$, indicating a compressibility reduction of ~20% due to interactions. More precisely, we find that the compressibility in the centre of the trap is reduced by 18% compared with a non-interacting gas at the same density and temperature. This percentage is comparable to the ratio of 21% between the interaction energy in a small volume V at the centre of the cloud, $g/2\,(N-1)n_\sigma^2 V$, and the total energy of a non-interacting Fermi gas at the same density, $3/5E_F n_\sigma V$. Clearly, without prior knowledge of the interaction parameter, one cannot distinguish between a colder or more repulsively interacting system. Having a full thermodynamic description at hand, as discussed in more detail later, we also perform global profile fits of the acquired images (see Fig. 5) to numerically calculated density distributions and find $T/T_F = 0.17 \pm 0.01$, which is in good agreement with the temperature derived from density noise measurements. We want to emphasize again that even though the two underlying physical mechanisms that lead to the observed suppression of density fluctuations are fundamentally different, it is impossible to distinguish these two contributions by performing density noise measurements alone at the given signal-to-noise ratio.

To unambiguously distinguish between temperature and interaction effects, we study the expansion dynamics of the cloud after being released from the trap. In addition to the kinetic energy of the gas, interactions provide a release energy that is mapped to momentum after a long time of flight. As the mean-field energy preferentially pushes atoms along the direction of the largest density gradient, this conversion produces an anisotropic distribution after a long time of flight (see Fig. 4a–c). The expansion can be described via scaling solutions of the time-dependent Boltzmann–Vlasov equation (see Methods)[49–52]. Unlike in trap, the effect of interactions on the density after expansion cannot be partly captured by a lower temperature, and result in a non-unity aspect ratio at long times. This is in stark contrast to the expansion behaviour of an ideal Fermi gas where expansion is purely ballistic and after a long time of flight reflects the isotropic momentum distribution even if the confining potential is anisotropic.

Figure 4d displays the aspect ratio of a SU(10) atom cloud measured after variable expansion times t_{tof} out of a harmonic trap with $\nu_r = 125\,\text{Hz}$ and $\nu_z = 800\,\text{Hz}$. The sample contains 50,000 atoms per spin component at $T/T_F = 0.16$. Initially, the atom cloud reproduces the trap's asymmetry. As $\nu_{r,z}t_{tof}$ becomes larger than 1, the spatial density distribution is determined more and more by the momentum distribution in the gas. Observing an inversion of the aspect ratio beyond 1 is an unambiguous signature of the interactions modifying the isotropic momentum distribution during time of flight[53].

To further explore this behaviour, we present in Fig. 4e measurements of the expanded cloud aspect ratio ($t_{tof} = 15.5\,\text{ms}$) as a function of the confinement asymmetry for a ten-component gas and a spin-polarized gas, both at $T/T_F = 0.16$. In the non-interacting case $N = 1$ (blue data points), the aspect ratio is always 1 as expected in the long time-of-flight limit. Finally, we show in Fig. 4f the dependence of the observed cloud aspect ratio on T/T_F for a fixed initial confinement with $\nu_r = 130\,\text{Hz}$ and $\nu_z = 725\,\text{Hz}$ and unchanged $t_{tof} = 15.5\,\text{ms}$. Atomic interactions include a mean-field term $\propto a$ and a collision integral $I_c(f) \propto a^2$; see equation (1). The latter, however, is only relevant in the presence of high collision rates and its pronounced effect is observed when the gas is relatively hot (Fig. 4f). In comparison, the interaction energy and kinetic energy become comparable at low temperatures, and the collisional rate is suppressed by Fermi statistics.

All measurements are well reproduced by our quantitative model (see Methods). To emphasize the role of N in modifying the dynamics, we also plot in Fig. 4d–f the behaviour expected for $N = 1, 4, 7, 10$ spin states using the validated theoretical model. As aspect ratio measurements via Gaussian fits are fairly immune to most imaging artifacts, they can be exploited to perform precise thermometry of the interacting Fermi gas.

Beyond their directly visible manifestation through cloud ellipticity, interaction-modified expansion dynamics can also be identified by carefully inspecting high-signal-to-noise-ratio absorption images. Figure 5 illustrates that a presumably round line-of-sight integrated density profile $n(x, z)$ still contains a systematic interaction signature. After $t_{tof} = 11.5\,\text{ms}$, we observe density profiles that at first sight appear circularly symmetric (first row) for the experimental data (first column), the non-interacting (second column) and the interacting models (third column). Interactions are revealed in the transpose anisotropy of the density distribution, defined as $n(x, z) - n(z, x)$, shown in the second row. Both the experimental data and the interacting model exhibit pronounced lobes that are not visible in the non-interacting case. Finally, a one-dimensional measure of this anisotropy can be defined by integrating over one of the axes ($\int dz(n(x, z) - n(z, x))$) as shown in the third row. In the integrated transpose anisotropy, we observe peaks symmetric to the centre of the cloud, the heights of which are sensitive to T/T_F for the experimental data and the interacting model, whereas in the non-interacting case this anisotropy is considerably reduced, inverted and insensitive to temperature. Thus, the anisotropy reveals the interacting nature of the Fermi gas in a single absorption image and can serve as a precise temperature probe.

Conclusions

We have demonstrated that SU(N) symmetry substantially enhances interaction dynamics in a quantum degenerate Fermi gas. This allows us to reach ultralow temperatures in short timescales. Creating a spin-polarized degenerate sample with a total preparation time under 3 s is important for the realization of atomic clocks probing engineered quantum states of matter[30]. The many-body problem for the dilute repulsively interacting Fermi gas can be solved exactly, and we have shown with high precision how the additional spin degree of freedom systematically modifies thermodynamic properties in the bulk gas. This opens a path to future quantum simulators capable of systematically exploring SU(N)-symmetric Fermi systems in periodic potentials.

Online content

Any methods, additional references, Nature Research reporting summaries, source data, extended data, supplementary information, acknowledgements, peer review information; details of author contributions and competing interests; and statements of data and code availability are available at https://doi.org/10.1038/s41567-020-0986-6.

References

1. Bloch, I., Dalibard, J. & Zwerger, W. Many-body physics with ultracold gases. *Rev. Mod. Phys.* **80**, 885–964 (2008).
2. Inguscio, M., Ketterle, W. & Salomon, C. (eds) *Making, Probing and Understanding Ultracold Fermi Gases* (IOS, 2008).
3. Cazalilla, M. & Rey, A. M. Ultracold fermi gases with emergent SU(N) symmetry. *Rep. Prog. Phys.* **77**, 124401 (2014).
4. Horikoshi, M., Nakajima, S., Ueda, M. & Mukaiyama, T. Measurement of universal thermodynamic functions for a unitary Fermi gas. *Science* **327**, 442–445 (2010).
5. Nascimbéne, S., Navon, N., Jiang, K., Chevy, F. & Salomon, C. Exploring the thermodynamics of a universal Fermi gas. *Nature* **463**, 1057–1060 (2010).
6. Gorshkov, A. V. et al. Two-orbital SU(N) magnetism with ultracold alkaline-earth atoms. *Nat. Phys.* **6**, 289–295 (2010).
7. Taie, S., Yamazaki, R., Sugawa, S. & Takahashi, Y. An SU(6) Mott insulator of an atomic Fermi gas realized by large-spin Pomeranchuk cooling. *Nat. Phys.* **8**, 825–830 (2012).
8. Scazza, F. et al. Observation of two-orbital spin-exchange interactions with ultracold SU(N)-symmetric fermions. *Nat. Phys.* **10**, 779–784 (2014).
9. Hofrichter, C. et al. Direct probing of the Mott crossover in the SU(N) Fermi-Hubbard model. *Phys. Rev. X* **6**, 021030 (2016).
10. Goban, A. et al. Emergence of multi-body interactions in a fermionic lattice clock. *Nature* **563**, 369–373 (2018).
11. Ozawa, H., Taie, S. & Takahashi, Y. Antiferromagnetic spin correlation of SU(N) Fermi gas in an optical lattice. *Phys. Rev. Lett.* **121**, 225303 (2018).
12. Zhang, X. et al. Spectroscopic observation of SU(N)-symmetric interactions in Sr orbital magnetism. *Science* **345**, 1467–1473 (2014).
13. Pagano, G. et al. A one-dimensional liquid of fermions with tunable spin. *Nat. Phys.* **10**, 198–201 (2014).
14. Song, B. et al. Evidence for bosonization in a three-dimensional gas of SU(N) fermions. Preprint at https://arxiv.org/abs/1912.12105 (2020).
15. He, C. et al. Collective excitations in two-dimensional SU(N) Fermi gases with tunable spin. *Phys. Rev. Res.* **2**, 012028 (2020).
16. Stellmer, S., Schreck, F. & Killian, T. C. in *Annual Review of Cold Atoms and Molecules* Ch. 1 (World Scientific, 2014).
17. Hazzard, K. R. A., Gurarie, V., Hermele, M. & Rey, A. M. High-temperature properties of fermionic alkaline-earth-metal atoms in optical lattices. *Phys. Rev. A* **85**, 041604 (2012).
18. Bonnes, L., Hazzard, K. R. A., Manmana, S. R., Rey, A. M. & Wessel, S. Adiabatic loading of one-dimensional SU(N) alkaline-earth-atom fermions in optical lattices. *Phys. Rev. Lett.* **109**, 205305 (2012).
19. Messio, L. & Mila, F. Entropy dependence of correlations in one-dimensional SU(N) antiferromagnets. *Phys. Rev. Lett.* **109**, 205306 (2012).
20. Yip, S.-K., Huang, J. & Kao, J. Theory of SU(N) fermi liquids. *Phys. Rev. A* **89**, 043610 (2014).
21. Campbell, S. L. et al. A Fermi-degenerate three-dimensional optical lattice clock. *Science* **358**, 90–94 (2017).
22. Marti, G. E. et al. Imaging optical frequencies with 100μHz precision and 1.1μm resolution. *Phys. Rev. Lett.* **120**, 103201 (2018).
23. Oelker, E. et al. Demonstration of 4.8×10^{-17} stability at 1 s for two independent optical clocks. *Nat. Photon.* **13**, 714–719 (2019).
24. McGrew, W. F. et al. Atomic clock performance enabling geodesy below the centimetre level. *Nature* **564**, 87–90 (2018).
25. Huntemann, N., Sanner, C., Lipphardt, B., Tamm, C. & Peik, E. Single-ion atomic clock with 3×10^{-18} systematic uncertainty. *Phys. Rev. Lett.* **116**, 063001 (2016).
26. Sanner, C. et al. Optical clock comparison for Lorentz symmetry testing. *Nature* **567**, 204–208 (2019).
27. Kolkowitz, S. et al. Gravitational wave detection with optical lattice atomic clocks. *Phys. Rev. D* **94**, 124043 (2016).
28. Xu, V., Jaffe, M., Panda, C., Clark, L. & Müller, H. Probing gravity by holding atoms for 20 seconds. *Science* **366**, 745–749 (2019).
29. Schioppo, M. et al. Ultrastable optical clock with two cold-atom ensembles. *Nat. Photon.* **11**, 48–52 (2017).
30. Hutson, R. B. et al. Engineering quantum states of matter for atomic clocks in shallow optical lattices. *Phys. Rev. Lett.* **123**, 123401 (2019).
31. Loftus, T., Ido, T., Ludlow, A., Boyd, M. & Ye, J. Narrow line cooling: finite photon recoil dynamics. *Phys. Rev. Lett.* **93**, 073003 (2004).
32. Stellmer, S., Grimm, R. & Schreck, F. Production of quantum-degenerate strontium gases. *Phys. Rev. A* **87**, 013611 (2013).
33. Julienne, P. S., Smith, A. M. & Burnett, K. in *Advances In Atomic, Molecular, and Optical Physics* Vol. 30 (eds Bates, D. & Bederson, B.) 141–198 (Academic, 1992).
34. Sesko, D. W., Walker, T. G. & Wieman, C. E. Behavior of neutral atoms in a spontaneous force trap. *J. Opt. Soc. Am. B* **8**, 946–958 (1991).
35. Stellmer, S., Pasquiou, B., Grimm, R. & Schreck, F. Laser cooling to quantum degeneracy. *Phys. Rev. Lett.* **110**, 263003 (2013).
36. Mukaiyama, T., Katori, H., Ido, T., Li, Y. & Kuwata-Gonokami, M. Recoil-limited laser cooling of ^{87}Sr atoms near the Fermi temperature. *Phys. Rev. Lett.* **90**, 113002 (2003).
37. Fukuhara, T., Takasu, Y., Kumakura, M. & Takahashi, Y. Degenerate Fermi gases of ytterbium. *Phys. Rev. Lett.* **98**, 030401 (2007).
38. Dick, G. J. *Local Oscillator Induced Instabilities in Trapped Ion Frequency Standards*. In *Proceedings of the 19th Annual Precise Time and Time Interval Meeting*, 133-147 (US Naval Observatory, 1988).
39. Sleator, T., Pfau, T., Balykin, V., Carnal, O. & Mlynek, J. Experimental demonstration of the optical Stern-Gerlach effect. *Phys. Rev. Lett.* **68**, 1996–1999 (1992).
40. Taie, S. et al. Realization of a SU(2) × SU(6) system of fermions in a cold atomic gas. *Phys. Rev. Lett.* **105**, 190401 (2010).
41. Stellmer, S., Grimm, R. & Schreck, F. Detection and manipulation of nuclear spin states in fermionic strontium. *Phys. Rev. A* **84**, 043611 (2011).
42. Lee, Y.-R. et al. Compressibility of an ultracold Fermi gas with repulsive interactions. *Phys. Rev. A* **85**, 063615 (2012).
43. Callen, H. & T.A., W. Irreversibility and generalized noise. *Phys. Rev.* **83**, 34–40 (1951).
44. Sanner, C. et al. Suppression of density fluctuations in a quantum degenerate Fermi gas. *Phys. Rev. Lett.* **105**, 040402 (2010).
45. Müller, T. et al. Local observation of antibunching in a trapped Fermi gas. *Phys. Rev. Lett.* **105**, 040401 (2010).
46. Danielewicz, P. Quantum theory of nonequilibrium processes, I. *Ann. Phys.* **152**, 239–304 (1984).
47. Kadanoff, L. P., Baym, G. & Pines, D. *Quantum Statistical Mechanics* 1st edn (CRC, 2019).
48. Pedri, P., Guéry-Odelin, D. & Stringari, S. Dynamics of a classical gas including dissipative and mean-field effects. *Phys. Rev.* **68**, 043608 (2003).
49. Giorgini, S., Pitaevskii, L. P. & Stringari, S. Theory of ultracold atomic Fermi gases. *Rev. Mod. Phys.* **80**, 1215–1274 (2008).
50. Menotti, C., Pedri, P. & Stringari, S. Expansion of an interacting fermi gas. *Phys. Rev. Lett.* **89**, 250402 (2002).
51. Castin, Y. & Dum, R. Bose-Einstein condensates in time dependent traps. *Phys. Rev. Lett.* **77**, 5315–5319 (1996).
52. Guéry-Odelin, D. Mean-field effects in a trapped gas. *Phys. Rev. A* **66**, 033613 (2002).
53. O'Hara, K. M., Hemmer, S. L., Gehm, M. E., Granade, S. R. & Thomas, J. E. Observation of a strongly interacting degenerate Fermi gas of atoms. *Science* **298**, 2179–2182 (2002).

Methods

Transparency laser. The transparency light is derived from an extended cavity diode laser that is filtered by a volume Bragg grating. Owing to amplified spontaneous emission, we see a lifetime in the dimple of 5 s. The beam is linearly polarized along x, and a small magnetic field is applied along z. To separately extract the number of atoms in the dimple and reservoir, the HODT is extinguished. Atoms in the dimple are guided by the VODT which has a small angle with respect to gravity, whereas atoms in the reservoir undergo free expansion. This spatially separates the atoms in the dimple and the reservoir, and atom numbers can be respectively counted through absorption imaging. T/T_F is then extracted for atoms in the dimple by calculating T_F and measuring the temperature, which is determined by fitting the reservoir and dimple atoms to a Gaussian fit after extinguishing the XODT after the long time of flight.

Three-body loss. To determine k_3, we load a thermal gas with $T = 1.45\,\mu K$ into the dimple part of the recompressed dipole trap. Starting from an initial central density of $n = 3.9 \times 10^{14}\,cm^{-3}$, we measure over the next 10 s a decay of the total atom number $\tilde{N}(t)$ as a function of the holding time t. The observed atom loss is modelled as

$$\tilde{N}(t) = \tilde{N}(0) - k_3 \int_0^t d\tau \int n^3(\mathbf{r}, \tau) dV \ , \tag{2}$$

where $n(\mathbf{r}, t)$ is the atomic density at position $\mathbf{r}$ and time t. We find $k_3 = 4.7(1.2) \times 10^{-30}\,cm^6\,s^{-1}$. This is a factor of 2 larger than the recent lattice-based three-body measurement that showed agreement with a universal van der Waals model[10]. Discrepancies in three-body loss between bulk gas measurements and predictions have been seen before[54,55], demonstrating the challenge in accounting for inhomogeneous density profiles. Under our experimental conditions, single- and two-body contributions are expected to be negligible over a time interval of 10 s and, using a corresponding model, we find them to be statistically insignificant.

TenS4 laser. The TenS4 laser overlaps with the VODT and the transparency beam, and has a 30 μm waist with a peak intensity of 0.15 kW cm^{-2}. The beam is linearly polarized along y, and along this axis a small magnetic field of 5 G is also applied, producing a small differential force between m_F states of opposite signs. Owing to our relatively small magnetic field and optical power, the TenS4 beam does not provide enough force to completely remove all other nuclear spin states. Consequently, we conventionally remove atoms with $m_F = -9/2$ and $m_F = -7/2$ before evaporation using optical pumping to aid with spin selectivity. To ensure that we are not addressing a molecular resonance, photoassociation spectra were measured at a variety of detunings from the $^3P_1$, $F = 11/2$ resonance. A low-finesse cavity is also used to filter out amplified spontaneous emission from the extended cavity diode laser that produces substantial on-resonant scattering.

Model. Our system is well described by the Hamiltonian

$$\begin{aligned} H \ &= \sum_\sigma \int d^3\mathbf{r} \ \hat{\psi}_\sigma^\dagger(\mathbf{r}) \left(-\frac{\nabla^2}{2m} + U(\mathbf{r}) \right) \hat{\psi}_\sigma(\mathbf{r}) \\ &+ \frac{g}{2} \sum_{\sigma,\sigma'} \int d^3\mathbf{r} \ \hat{\psi}_\sigma^\dagger(\mathbf{r}) \hat{\psi}_{\sigma'}^\dagger(\mathbf{r}) \hat{\psi}_{\sigma'}(\mathbf{r}) \hat{\psi}_\sigma(\mathbf{r}) \end{aligned} \tag{3}$$

where $\hat{\psi}_\sigma(\mathbf{r})$ ($\hat{\psi}_\sigma^\dagger(\mathbf{r})$) annihilates (creates) a fermion of spin σ at point $\mathbf{r}$. The fermions are confined by a harmonic trapping potential $U = m/2 \sum_i (2\pi\nu_i)^2 x_i^2$ and interact via SU(N)-symmetric s-wave contact interactions of strength g, given in terms of a and m.

Kinetic approach. To study the collective behaviour of the quantum gas, we use a kinetic approach[46,47] considering the semi-classical phase-space distribution $f_{\sigma,\sigma'}(\mathbf{r}, \mathbf{p})$ defined as

$$f_{\sigma,\sigma'}(\mathbf{r}, \mathbf{p}) = \int d^3\mathbf{r}' e^{i\mathbf{p}\cdot\mathbf{r}'} \langle \hat{\psi}_\sigma^\dagger(\mathbf{r} + \mathbf{r}') \hat{\psi}_{\sigma'}(\mathbf{r} - \mathbf{r}') \rangle \tag{4}$$

in terms of the fermionic creation/annihilation operators. The real-space atomic density is then given by $n_\sigma(\mathbf{r}) = \int d^3\mathbf{p} f_{\sigma,\sigma}(\mathbf{r}, \mathbf{p})$.

We will further assume that the Wigner function is purely diagonal in the spin indices (that is, we will neglect any off-diagonal contributions) and as the experiment prepares an equal number of atoms in each spin state, that the diagonal terms are all equal: $f_{\sigma,\sigma'} = \delta_{\sigma,\sigma'} f$.

Finally, we will treat the interparticle interaction in the mean-field approximation assuming an interaction energy

$$V_{MF} = g(N-1)n(\mathbf{r}) \tag{5}$$

which is directly proportional to the real-space density $n(\mathbf{r})$, g and $N-1$.

With these approximations, the collisional Boltzmann–Vlasov equation reads as in equation (1) in the main text.

Relaxation time approximation. Instead of a detailed treatment of the collisions between particles, we employ the relaxation time approximation[48], which approximates

$$I_c[f] = -\frac{f - f_{le}}{\tau} \ , \tag{6}$$

where f approaches the local equilibrium state f_{le} over a characteristic relaxation time τ.

We follow refs. [56,57] and approximate the relaxation time as

$$(2\pi\nu\tau)^{-1} = (N-1)\frac{4}{5\,3^{1/3}\pi} \left(\tilde{N}^{1/3} \frac{a}{a_{ho}} \right)^2 F_Q(T/T_F) \ , \tag{7}$$

where $F_Q(T/T_F)$ is a universal function of T/T_F, as defined in ref. [56], and a_{ho} is the harmonic oscillator length. F_Q vanishes as $(T/T_F)^2$ at low temperatures, a signature of Fermi statistics, is of order 1 in the intermediate temperature regime and vanishes as $(T/T_F)^{-1}$ at higher temperatures.

Equilibrium solution. Solving the Boltzman–Vlasov equation in equilibrium, we obtain

$$f(\mathbf{r}, \mathbf{p}) = \frac{1}{e^{\beta\left(\frac{p^2}{2m} + U(\mathbf{r}) + g(N-1)n(\mathbf{r}) - \mu\right)} + 1} , \tag{8}$$

which has to be solved self-consistently, as it depends on $n(\mathbf{r}) = \int \frac{d^3\mathbf{p}}{(2\pi\hbar)^3} f(\mathbf{r}, \mathbf{p})$.

In practice, we solve $f(\mathbf{r}, \mathbf{p})$ iteratively in steps i. We start by ignoring the interaction term, and determine μ_0 from $\int \frac{d^3\mathbf{r} d^3\mathbf{p}}{(2\pi\hbar)^3} f(\mathbf{r}, \mathbf{p}) = N_\sigma$ where N_σ is the number of atoms per spin species that defines f_0. Having f_{i-1}, we compute the density n_i and the corresponding interaction energy $V_{MF,i}$. This defines $f(\mu_i, V_{MF,i})$ from which we determine μ_i via normalization. We then set $f_i = \alpha f(\mu_i, V_{MF,i}) + (1-\alpha)f_{i-1}$ with $\alpha = 0.9$. Iterating this procedure leads to convergence in 5–10 iterations for the parameters we consider.

Number fluctuations. We can compute the expected number fluctuations directly from the obtained density profiles. The fluctuation–dissipation theorem describes how the number fluctuations of the gas are related to the isothermal compressibility: $\Delta \tilde{N}^2/\tilde{N} = nk_B T\kappa$, where the isothermal compressibility $\kappa = \frac{1}{n^2}\frac{\partial n}{\partial \mu}$.

In the harmonic trap the chemical potential varies as $\mu(\mathbf{r}) = \mu - U(\mathbf{r})$. Thus, the derivative with respect to μ can be replaced by a derivative with respect to one of the spatial directions as $\frac{\partial n}{\partial \mu} = \frac{-1}{m(2\pi\nu_i)^2 r_i}\frac{\partial n}{\partial r_i}$, which we can directly evaluate based on the computed density profiles.

Dynamics. To obtain the dynamics we use the scaling factor method[48–52] with the ansatz

$$f(\mathbf{r}, \mathbf{p}, t) = \frac{1}{\prod_j (\lambda_j \theta_j^{1/2})} f_0 \left(\frac{r_i}{\lambda_i}, \frac{1}{\theta_i^{1/2}}(p_i - m\dot\lambda/\lambda_i r_i) \right) \tag{9}$$

for the out-of-equilibrium distribution function of the gas, where $i = x, y, z$ labels the spatial directions.

Following[48], we take the moments of $r_i p_i$ and p_i^2 to obtain a closed set of differential equations for the scaling parameters λ_i and θ_i:

$$\begin{aligned} \ddot\lambda_i + (2\pi\nu_i)^2 \lambda_i - (2\pi\nu_i)^2 \frac{\theta_i}{\lambda_i} \\ + (2\pi\nu_i)^2 \xi_i \left(\frac{\theta_i}{\lambda_i} - \frac{1}{\lambda_i \prod_j \lambda_j} \right) = 0 \ , \end{aligned} \tag{10}$$

and

$$\dot\theta_i + 2\frac{\dot\lambda_i}{\lambda_i}\theta_i = -(\theta_i - \overline{\theta})/\tau \ , \tag{11}$$

where $\xi_i = \frac{g/2(N-1)<n>}{g/2(N-1)<n> + <p_i^2>/m}$ accounts for the mean-field interaction with $<\cdots>$ being phase-space averages with respect to the equilibrium distribution, dotted variables refer to their time derivatives and $\overline{\theta} = 1/3\sum_i \theta_i$.

Time of flight. To study the expansion after switching off the trap, the second term in equation (10) is set to 0, and the nonlinear coupled differential equations are solved for the scaling parameters, which, when plugged into the scaling ansatz, yield the phase-space distribution after time of flight.

For the non-interacting case, the equations for the expansion can be solved explicitly. In the collisionless regime, $\theta_i = \lambda_i^{-2}$ and the equation for λ_i can be solved to obtain $\lambda_i^{(0)}(t) = \sqrt{1 + (2\pi\nu_i)^2 t^2}$. Using the non-interacting value of the initial root mean square radii, $<x_i^2>_0 (t=0) = \frac{k_B T}{m(2\pi\nu_i)^2}$, we obtain after time of flight $<x_i^2>_0 (t) = \frac{k_B T}{m}\frac{1 + (2\pi\nu_i)^2 t^2}{(2\pi\nu_i)^2}$, such that the ratio of different directions approaches 1, and the cloud becomes isotropic.

Virial expansion for the number fluctuations. An alternative approach to derive the thermodynamic quantities is provided by virial expansions of the partition function of the interacting many-body system[58–60].

As we are interested in the number fluctuations, and thus κ, we start from the expression for the chemical potential of a homogeneous Fermi gas at low temperature and weak interactions[61], adapted to the SU(N) case

$$
\begin{aligned}
\mu(n, T, a) \quad = E_F \Big[1 - \tfrac{\pi^2}{12}(T/T_F)^2 + \tfrac{4}{3\pi}(N-1)k_F a \\
+ \tfrac{4(11-2\ln(2))}{15\pi^2}(k_F a)^2 (N-1) \Big] + CT^2 a^2 \; ,
\end{aligned}
\tag{12}
$$

where C is a constant independent of n. We can then evaluate the compressibility from the dependence of n on the Fermi parameters.

For simplicity we only keep terms up to first order, to obtain for $\Delta \tilde{N}^2 / \tilde{N}$ the equation presented in the main text.

Data availability

The datasets generated and analysed during the current study are available from the corresponding author L.S. on reasonable request.

References

54. Burt, E. A. et al. Coherence, correlations, and collisions: what one learns about Bose-Einstein condensates from their decay. *Phys. Rev. Lett.* **79**, 337–340 (1997).
55. Wolf, J. et al. State-to-state chemistry for three-body recombination in an ultracold rubidium gas. *Science* **358**, 921–924 (2017).
56. Vichi, L. Collisional Damping of the Collective Oscillations of a Trapped Fermi Gas. *J. Low Temp. Phys.* **121**, 177–197 (2000).
57. Jackson, B., Pedri, P. & Stringari, S. Collisions and expansion of an ultracold dilute Fermi gas. *Europhys. Lett.* **67**, 524–530 (2004).
58. Lee, T. D. & Yang, C. N. Many-body problem in quantum statistical mechanics. I. General formulation. *Phys. Rev.* **113**, 1165–1177 (1959).
59. Lee, T. D. & Yang, C. N. Many-body problem in quantum statistical mechanics. II. Virial expansion for hard-sphere gas. *Phys. Rev.* **116**, 25–31 (1959).
60. Lee, T. D. & Yang, C. N. Many-body problem in quantum statistical mechanics. III. Zero-temperature limit for dilute hard spheres. *Phys. Rev.* **117**, 12–21 (1960).
61. Pathria, R. K. & Kawatra, M. P. Quantum statistical mechanics of a many-body system with square-well interaction. *Progr. Theor. Phys.* **27**, 638–652 (1962).

Author contributions

L.S., C.S., R.B.H., A.G., L.Y., W.R.M. and J.Y. contributed to the experimental measurements. T.B. and A.M.R. developed the theoretical model. All authors discussed the results, contributed to the data analysis and worked together on the manuscript.

Competing interests

The authors declare no competing interests.

Additional information

Correspondence and requests for materials should be addressed to L.S. or J.Y.

Peer review information *Nature Physics* thanks Stefano Giorgini, Florian Schreck and the other, anonymous, reviewer(s) for their contribution to the peer review of this work.

Reprints and permissions information is available at www.nature.com/reprints.